Forward Modeling of the Phobos Tides and Applications to the First Martian Year of the InSight Mission

L. Pou, F. Nimmo, P. Lognonné, D. Mimoun, R. Garcia, B. Pinot, A. Rivoldini, D. Banfield, W. Banerdt

To cite this version:

L. Pou, F. Nimmo, P. Lognonné, D. Mimoun, R. Garcia, et al.. Forward Modeling of the Phobos Tides and Applications to the First Martian Year of the InSight Mission. Earth and Space Science, 2021, 8 (7), 10.1029/2021ea001669 . hal-03540523

HAL Id: hal-03540523

https://hal.science/hal-03540523v1

Submitted on 24 Jan 2022

Earth and Space Science

RESEARCH ARTICLE
10.1029/2021EA001669

Key Points:

- The Phobos tides of degree 2, 3, and 4 should be detectable by the Very Broad Band seismometer on InSight's Seismic Experiment for Interior Structure (SEIS)
- We model these tides, the Martian interior and SEIS low frequency noise with recent InSight data
- Over 2 Earth years, determining the core state and size with 125 km accuracy should be possible

Correspondence to:
L. Pou,
lpou@ucsc.edu

Citation:
Pou, L., Nimmo, F., Lognonné, P., Mimoun, D., Garcia, R. F., Pinot, B., et al. (2021). Forward modeling of the Phobos tides and applications to the first Martian year of the InSight mission. *Earth and Space Science*, *8*, e2021EA001669. https://doi.org/10.1029/2021EA001669

Received 21 JAN 2021
Accepted 1 JUN 2021

Forward Modeling of the Phobos Tides and Applications to the First Martian Year of the InSight Mission

L. Pou[1], F. Nimmo[1], P. Lognonné[2], D. Mimoun[3], R. F. Garcia[3], B. Pinot[3], A. Rivoldini[4], D. Banfield[5], and W. B. Banerdt[6]

[1]Department of Earth and Planetary Sciences, University of California Santa Cruz, Santa Cruz, CA, USA, [2]Université de Paris, Institut de physique du globe de Paris, CNRS, Paris, France, [3]Institut Supérieur de l'Aéronautique et de l'Espace SUPAERO, Toulouse, France, [4]Royal Observatory of Belgium, Brussels, Belgium, [5]Cornell Center for Astrophysics and Planetary Science, Cornell University, Ithaca, NY, USA, [6]Jet Propulsion Laboratory, California Institute of Technology, Pasadena, CA, USA

Abstract The tidal response of Mars, due to the Sun and the Martian moons, Phobos and Deimos, provides information about the interior structure of Mars. By using the Very Broad Band (VBB) seismometer of Seismic Experiment for Interior Structure (SEIS) as a gravimeter on the surface of Mars, the InSight mission will provide the long-period data suited to tidal analysis: most notably, the proximity of Phobos implies that degree 2, 3, 4, and further tides will be detectable by the VBB and are expected to provide information about the rheology at different depths within Mars. In order to expedite the recovery of these tidal signals in the SEIS measurements, we model the tides raised by Phobos using a tidal potential deduced from JPL Horizons ephemerides. From this potential, we calculate the expected tidal acceleration at InSight's location and gravimetric factors using a set of plausible interior models of Mars. To simulate the expected long period signal on the VBB seismometer, we use the InSight Auxiliary Payload Sensor Suite data to model the noise seen at low frequency by SEIS mainly due to temperature and pressure variations. Based on this synthetic signal, by applying filtering methods such as stacking and matched filtering to these synthetic data, we show that by recovering the gravimetric factors, it should be possible to constrain the state of the core and its size with an accuracy of 125 km after two Earth years.

Plain Language Summary On Mars since November 26, 2018, the NASA InSight mission made weather measurements of the atmosphere's temperature, wind, and pressure. It has also put a seismometer at the surface of Mars to see Mars quakes. However, the seismometer can also be used to measure the tides due to the Martian moon Phobos: by deforming the surface of the planet, the Phobos tides will create a change in the gravity at the surface of Mars, which can be recorded. As Phobos is closer to Mars than the Moon is to Earth, the shape of the tides on Mars is more complicated, but can be used to determine the interior structure of Mars. In particular, its deepest part, the core, is not well determined: it is still unsure whether it is liquid or solid, and how big it is. We model the expected tides at InSight's location and noises due to temperature and pressure variations based on the measurements made to guess what the seismometer will record. This study shows that after two Earth years, we should be able to see the Phobos tides accurately enough to know the core state and size with an accuracy of 125 km.

1. Introduction

The tides of Phobos raised on Mars can help constraining the internal structure of Mars (Bills et al., 2005; Lognonné & Mosser, 1993). The tidal response of Mars contains information about its internal structure (e.g., Van Hoolst et al., 2003), its thermophysical properties (e.g., Nimmo & Faul, 2013) and the temperature and rheology governing it (e.g., Bagheri et al., 2019). While the Sun is the cause of the largest tides on Mars, these solar tides have the same period as diurnal temperature and pressure variations (Spiga et al., 2018): this makes measuring the Martian response to the solar tides from the Martian surface extremely challenging (Van Hoolst et al., 2003). However, tides raised by Phobos are in a different frequency range and for this reason less affected by atmospheric signals of diurnal periods (e.g., Lognonné et al., 1996) and therefore more suitable to be measured by an instrument on the surface, Additionally, due to the proximity of Phobos to Mars, tides of higher harmonic degree might be detectable as well. Since the harmonic degree affects the sounding depth of tides, measuring tides of higher harmonics is an effective way to deduce information about the planet interior (Lognonné et al., 2019). The Seismic Experiment for Interior Structure instrument (SEIS) of the InSight mission, when being used as a gravimeter on the surface of Mars, has a resolution that is good enough to be able to detect the gravitational signature induced by Phobos tides of degree 2, 3, and 4 (Lognonné et al., 2019). However, the accelerations measured by SEIS require advanced signal processing in order to remove the environmental noise mainly due to surface pressure and temperature variations (Mimoun et al., 2017; Pou et al., 2018).

In this paper, we construct a forward model of the Phobos tides up to a degree $\ell = 4$, and update the noise model experienced by SEIS (based on previous works from Mimoun et al., 2017 and Pou et al., 2018) at low frequencies with the new environmental data measured with InSight's Auxiliary Payload Sensor Suite (APSS) at the surface of Mars (Banerdt et al., 2020; Banfield et al., 2020). To characterize the tidal response of Mars induced by Phobos, we compute Love numbers for a set of plausible interior models of Mars (Rivoldini et al., 2011; Smrekar et al., 2018; G. J. Taylor, 2013; Yoshizaki & McDonough, 2020). From the tidal signature and from our noise model we generate a simulated SEIS output at low frequency as measured by its broadband instrument, the Very Broad Band (VBB) seismometer. We then apply the recovery method detailed in Pou et al. (2018) and show that from the measured amplitudes of the Phobos tides, the Martian core size and state can be determined by accumulating two Earth years of data. Finally, we corroborate our findings with the real SEIS data from the first Martian year recorded by InSight. While the decorrelation process is currently less effective due to nonlinear effects, the current trend indicates that the real Phobos tides should be detectable enough to constrain the core radius with two Earth years' worth of the data.

2. Tidal Potential of Phobos

By orbiting Mars, Phobos causes a gravitational pull on the planet, which responds to this external forcing by deforming in the form of a tidal bulge. The response of Mars is a function of its internal structure and of the tidal potential of Phobos, which can be expressed as a sum of Legendre polynomials (Kaula, 1964):

$$V(r) = \frac{Gm^*}{a^*} \sum_{\ell=2}^{\infty} \left(\frac{r}{a^*}\right)^{\ell} P_\ell\left(\cos S\right) \tag{1}$$

where G is the gravitational constant, m^* and a^* the mass and the semi-major axis of Phobos, and P_ℓ the Legendre polynomial of degree ℓ. r is the distance between the center of Mars and the point where the tidal potential V is calculated, and S is the solid angle between the axis linking the center of Mars to the aforementioned point and the sub-Phobos point on the Martian surface.

For a distant body such as the Moon to the Earth or the Sun to Mars, because of the $\frac{r}{a^*}$ term, only degree 2 is usually considered. For the Sun to Mars, its value is around 10^{-5}; however, for Phobos this term is roughly equal to 0.36 (using values from Jacobson & Lainey, 2014; Seidelmann et al., 2007). Given their large contribution, the higher degree tides thus need to be considered (Bills et al., 2005).

In this work, we use the Phobos ephemerides mar097 from the JPL Horizons software over two full Earth years (2019–2020) to retrieve the cartesian coordinates of Phobos in the Martian barycenter reference frame. The time sampling has been chosen to be 1 s in order to fit the nominal sampling rate of SEIS at low frequencies.

We convert these cartesian coordinates into spherical coordinates in order to retrieve the colatitude θ and longitude ϕ of the sub-Phobos point. The angles are used to calculate the ground-track of Phobos over the 2 years (see Figure 1). With the ground-track of Phobos and the position of the InSight lander (4.502°N, 135.623°E, from the HiRise images; Golombek et al., 2020), the solid angle S between InSight and Phobos is calculated; the differences in position between the HiRise images and the RiSE measurements described in Golombek et al. (2020) do not change the value of S significantly. Equation 1 is then used to obtain the tidal potential of Phobos, assuming a semi-major axis of Phobos $a^* = 9{,}375$ km from Jacobson and Lainey (2014), a mean radius of Mars of $r = 3389.5$ km from Seidelmann et al. (2007) and $Gm^* = 0.7072 \times 10^{-3}$ km^3.s^{-2} for Phobos from Pätzold et al. (2014). From this tidal potential is thus derived the tidal acceleration due to Phobos at the surface of Mars, shown in Figure 1.

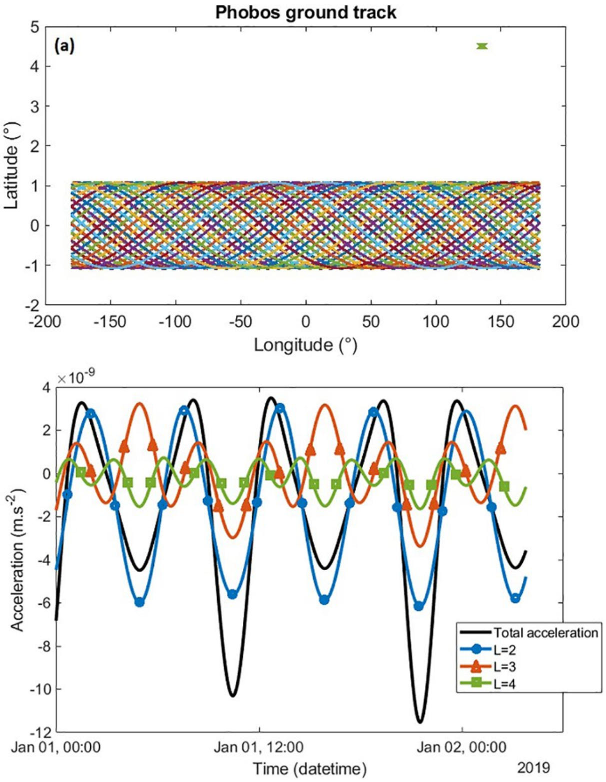

Figure 1. Phobos position over the Martian surface and forcing derived from the Phobos ephemerides mar097. (a) Ground-track of Phobos on the surface of Mars for the Earth years 2019 and 2020. The position of the InSight lander is indicated with a green cross at the top right of the figure. Due to changes in the Mars-Phobos distance and longer-period variations (such as apsidal precession (e.g., Jacobson & Lainey, 2014), the Phobos ground-track does not exactly repeat itself. To distinguish the trace of Phobos on the Martian surface, each transit has been given a different color. (b) Tidal acceleration due to the tidal potential of Phobos for degree 2, 3, and 4. Black line represents the total tidal acceleration. Degree 2 is the greatest tide with a period of 5.55 h, followed by degree 3 with a period of 3.70 h and then degree 4 with a period of 2.78 h.

This tidal forcing from Phobos distorts the shape of Mars, creating displacements, changes in gravitational potential, and variations of surface gravity. The tidal response of Mars is quantified by the Love numbers h, k, and l (Love, 1911; Shida, 1912), which depend on the internal structure and rheology of the planet, and are function of frequency f (e.g., Efroimsky & Lainey, 2007). These numbers are used to compute the gravitational factor δ, characterizing the change in local gravity due to the direct attraction of Phobos and the changes caused by Phobos to Mars. Neglecting small effects from non-sphericity, the gravimetric factor can be written as a linear combination of the Love numbers k and h (e.g., Agnew, 2007; Beuthe, 2015; Dehant et al., 1999):

$$\delta_\ell(f) = 1 - \frac{\ell+1}{\ell} k_\ell(f) + \frac{2}{\ell} h_\ell(f) \tag{2}$$

where ℓ is the degree of the tide considered. Hence, to compute the actual values of these parameters and determine the tidal response of Mars to the Phobos tides, it is necessary to model carefully the interior of Mars.

3. Mars Interior Modeling

While the various missions to Mars have arguably made it the best-known planet after the Earth, its internal structure has yet to be well-constrained (Smrekar et al., 2018). The bulk chemical composition of Mars has been deduced from the composition of Martian meteorites (McSween, 1994) and the data acquired by an orbiting spacecraft (e.g., Boynton et al., 2004), and assumptions about how Mars formed from the solar nebula. The gravitational response of Mars to the solar tides has been measured from orbiters (Yoder et al., 2003) with its most recent value $k_2^s = 0.174 \pm 0.008$ (Konopliv et al., 2020) having been used to argue for a liquid core. Together with its bulk density and moment of inertia, these parameters have been used to constrain the Martian interior structure (e.g., Bagheri et al., 2019; Folkner et al., 1997, Rivoldini et al., 2011). The secular acceleration of Phobos can be used to infer the tidal dissipation within Mars by constraining the dissipation factor or quality factor Q at the main Phobos tide (degree $\ell = 2$, or 19,980 s) (Bills et al., 2005; Khan et al., 2018; Lainey et al., 2007; Nimmo & Faul, 2013), and can also constrain its thermal evolution (Samuel et al., 2019).

Here, we will focus on determining the state and size of the Martian core through the measurement of the tidal gravimetric factors by the SEIS instrument. The first set of models, labeled TAY, is based on the Martian composition of G. J. Taylor (2013), using a more extended Martian meteorite database than Dreibus and Wanke (1985) and matching the composition with surface measurements, like the gamma ray spectrometer of Mars Odyssey (Boynton et al., 2004). We combine it with a rheology model based on the experimental data from Faul and Jackson (2007) for dry olivine and a mantle temperature structure based on the hot end-member of Plesa et al. (2018), also used in Smrekar et al. (2018). The mantle grain size was adjusted to fit the possible values of the dissipation factor Q_2^s from Smrekar et al. (2018) and Khan et al. (2018) with extreme values of $Q = 80$ (TAY1) and $Q = 105$ (TAY2), giving grain sizes of 24 and 58 mm respectively, so that the measured secular acceleration of Phobos is within our bounds. In order to roughly match the k_2^s measurements from Konopliv et al. (2011) ($k_2^s = 0.164 \pm 0.009$), Konopliv et al. (2016) ($k_2^s = 0.169 \pm 0.006$), and Konopliv et al. (2020) ($k_2^s = 0.174 \pm 0.008$), a liquid core was assumed with a radius between 1,600 and 1,850 km.

Table 1
Summary of the Key Parameters and References for the Martian Models Used in This Work With Their Labels

Label	Composition	Temperature	k_2^s range	Core range	Grain size
TAY1	G. J. Taylor (2013)	Case16 of Plesa et al. (2018)	0.139–0.184	1600–1850 km Liquid	24 mm
TAY2	G. J. Taylor (2013)	Case16 of Plesa et al. (2018)	0.139–0.184	1600–1850 km Liquid	58 mm
YOCold1	Yoshizaki and McDonough (2020)	Case 22 of Plesa et al. (2018)	0.134–0.183	1600–1850 km Liquid	5 mm
YOCold2	Yoshizaki and McDonough (2020)	Case 22 of Plesa et al. (2018)	0.134–0.183	1600–1850 km Liquid	10 mm
YOHot1	Yoshizaki and McDonough (2020)	Case 16 of Plesa et al. (2018)	0.134–0.183	1600–1850 km Liquid	24 mm
YOHot2	Yoshizaki and McDonough (2020)	Case 16 of Plesa et al. (2018)	0.134–0.183	1600–1850 km Liquid	58 mm
Solid	Nimmo and Faul (2013)	Nimmo and Faul (2013)	≤0.140	1600–1850 km Liquid	10 mm

The second set of models is based on the Martian composition from Yoshizaki and McDonough (2020), using the current knowledge of the composition of the solar nebula and meteorites at the time of Mars' accretion. For this composition we use either the hot temperature end-member of Plesa et al. (2018) (labeled YOHot, or Case 16 in the reference paper) or a profile intermediate between the hot and cold end-member of Plesa et al. (2018) (labeled YOCold, or Case 22). The rheology model is also based on the experimental data from Faul and Jackson (2007), and the grain size is set to respectively 5 and 10 mm for YOCold1 and YOCold2 and 24 and 58 mm for YOHot1 and YOHot2. The core is also assumed to be liquid, with a radius between 1,600 and 1,850 km.

Finally, a solid core model has also been developed, modified from the work of Nimmo and Faul (2013) with a potential mantle temperature of 1650 K, an elastic thickness of 125 km and a grain size of 10 mm. We also choose a solid core radius between 1,600 and 1,850 km to test whether measuring the Phobos tides would also be able to distinguish between a Martian solid core and a Martian liquid core. This solid core model is however not favored as its k_2^s values are always smaller than the k_2^s measurements from the solar tides in Konopliv et al. (2011, 2016, 2020).

The key parameters and references of our Martian models are summarized in Table 1.

4. Tidal Response of Mars to Phobos

Due to the tidal forcing of Phobos described in Section 2, the surface of Mars deforms, and the gravity measured at its surface also changes. The change in gravity is given by Stacey (1969):

$$\Delta g(r) = \sum_{\ell=2}^{\infty} \delta_\ell(f) \left(\ell g_0 \frac{m^*}{m_{Mars}} \left(\frac{r}{a^*} \right)^{\ell+1} P_\ell \left(\cos S \right) \right) \tag{3}$$

where g_0 is the surface acceleration due to gravity and m_{Mars} is the mass of Mars.

To correctly estimate the gravity changes at the surface of Mars, we must go back to the definition of the tidal potential given in Equation 1. This equation can be rewritten in terms of colatitude and longitude of the Martian point (θ, ϕ) and in Keplerian elements of the Phobos orbit with inclination i^*, eccentricity e^*, argument of the periapsis ω^*, argument of the ascending node Ω^* and mean anomaly M^* (Kaula, 1964):

$$\begin{aligned} V = {} & \frac{Gm^*}{a^*}\sum_{\ell=2}^{\infty}\left(\frac{r}{a^*}\right)^{\ell}\sum_{m=0}^{\ell}\frac{(\ell-m)!}{(\ell+m)!}(2-\delta_{0m})P_{\ell m}\left(\cos\theta\right)\sum_{p,q}F_{\ell mp}(i^*)G_{lpq}(e^*) \\ & \times\Bigg(\cos m\phi\begin{Bmatrix}\cos\\ \sin\end{Bmatrix}_{\ell-m\ \text{odd}}^{\ell-m\ \text{even}}\Big((\ell-2p)\omega^* + (\ell-2p+q)M^* + m(\Omega^*)\Big) \\ & +\sin m\phi\begin{Bmatrix}\sin\\ \cos\end{Bmatrix}_{\ell-m\ \text{odd}}^{\ell-m\ \text{even}}\Big((\ell-2p)\omega^* + (\ell-2p+q)M^* + m(\Omega^*)\Big)\Bigg) \end{aligned} \tag{4}$$

Here, ℓ is called the degree of the considered tide, and m is the order of the tide. $F_{\ell mp}(i^*)$, $G_{\ell pq}(e^*)$ are polynomial functions of respectively the inclination and eccentricity of Phobos. Because of the negligible inclination and eccentricity of Phobos $i = 0.046°$ and $e = 0.0151$ (Jacobson & Lainey, 2014), it is possible to consider only the order 0 in inclination and eccentricity in Equation 4 for the polynomials $F_{\ell mp}$ and $G_{\ell pq}$.

For degree 2, only the terms $\ell mpq = 2200$ and $\ell mpq = 2010$ are not null at order 0, giving the following tidal potentials:

$$V_{2200} = \frac{3}{4}\frac{Gm^*\ r^2}{a^{*3}}(1-\cos^2\theta)\Big(\cos(2\omega^* + 2M^* + 2\Omega^* - 2\phi)\Big) \tag{5}$$

$$V_{2010} = -\frac{Gm^*\ r^2}{a^{*3}}\frac{1}{4}(3\cos^2\theta - 1) \tag{6}$$

Adding them gives the resulting potential:

$$\begin{aligned} V_2(r) &= V_{2200} + V_{2010} \\ &= \frac{Gm^*}{a^*}\left(\frac{r}{a^*}\right)^2\frac{1}{4}\Big(3(1-\cos^2\theta)\cos(2\omega^* + 2M^* + 2\Omega^* - 2\phi) - 3\cos^2\theta + 1\Big) \\ &= \frac{Gm^*}{a^*}\left(\frac{r}{a^*}\right)^2\frac{1}{4}\Big(3(2\sin^2\theta\cos^2(\omega^* + M^* + \Omega^* - \phi) - 1) + 1\Big) \end{aligned} \tag{7}$$

With our assumption of negligible inclination and eccentricity of Phobos, we can rewrite the colatitude and longitude of InSight (θ, ϕ) and the longitude of Phobos $(\omega^* + M^* + \Omega^*)$ as the solid angle S:

$$\begin{aligned} V_2(r) &= \frac{Gm^*}{a^*}\left(\frac{r}{a^*}\right)^2\frac{1}{4}\Big(3(2\cos^2(S) - 1) + 1\Big) \\ &= \frac{Gm^*}{a^*}\left(\frac{r}{a^*}\right)^2\frac{1}{4}\Big(3\cos(2S) + 1\Big) \\ &= \frac{Gm^*}{a^*}\left(\frac{r}{a^*}\right)^2 P_2\left(\cos S\right) \end{aligned} \tag{8}$$

Which is Equation 1 for degree $\ell = 2$. As such, the order m of the tide corresponds to the argument of the cosine in the Legendre polynomial of degree ℓ: $\ell mpq = 2200$ corresponds to the term with $3\cos(2S)$, while $\ell mpq = 2010$ corresponds to the constant term in Equation 8. The same correspondence can be made for degree 3 and 4, with the respective Legendre polynomials:

$$\begin{aligned} P_3(\cos(S)) &= \frac{1}{8}\Big(5\cos(3S) + 3\cos(S)\Big) \\ P_4(\cos(S)) &= \frac{1}{64}\Big(35\cos(4S) + 20\cos(2S) + 9\Big) \end{aligned} \tag{9}$$

corresponding to tides $\ell mpq = 3300, 3110, 4400, 4210$, and 4020. This is in accordance with the footnote 9 in P. A. Taylor and Margot (2010), where they investigated the effects of high degree tides for binary systems. The degree 3 tide pattern has two components: one with a period equal Phobos synodic period of $T_1 = 11$ h 06 min from the $\cos(S)$ term and another with a periodicity of $T_3 = 3$ h 42 min, with the latter being the one with the greater amplitude. The degree 4 tide pattern also has two components, the largest amplitude being at $T_4 = 2$ h 47 min, but also a term at $T_2 = 5$ h 33 min, which is the same period as the periodicity of the $\ell = 2$ Phobos tides. This overlapping pattern will create interference and be an issue when trying to separate the different degrees contributions in the data.

We can rewrite the gravimetric factor from Equation 2:

$$\delta_{\ell mpq} = 1 - \frac{\ell + 1}{\ell} k_{\ell mpq} + \frac{2}{\ell} h_{\ell mpq} \tag{10}$$

The frequency dependency of the Love numbers is indicated by the order m of each term for the tidal potential of degree ℓ. For degree $\ell = 2$, only $m = 2$ corresponding to the period T_2 is used. However, for degree 3, we have to consider $m = 3$ but also $m = 1$. This means that the Love numbers must be calculated at both periods T_1 and T_3, written in our notations $\delta_3(T_1)$ and $\delta_3(T_3)$ (or δ_{3110} and δ_{3300}). The same can be said for degree 4 with periods T_4 and T_2.

In an elastic case, the solid angle S between Phobos and InSight would be perfectly in phase. However, in reality, Mars must be modeled as a viscoelastic body. Because of tidal dissipation from viscous effects, the tidal bulge of Mars will be misaligned with Phobos by an angle called the lunar-tidal interval (Redmond & Fish, 1964), or geometric lag angle (MacDonald, 1964). This is expressed as a phase lag ϵ to be added to the solid angle S inside the Legendre polynomials in Equation 1 (Kaula, 1964). This angle depends on the internal structure of Mars and more particularly on internal dissipation, characterized by the quality factor Q (e.g., Efroimsky & Makarov, 2013; Murray & Dermott, 2000), also frequency dependent (Efroimsky & Lainey, 2007; P. A. Taylor & Margot, 2010). The phase lag writes as:

$$\epsilon_{\ell mpq} = \frac{1}{Q_{\ell mpq}} = m\gamma_{\ell mpq}, \tag{11}$$

where γ is the geometric lag angle between the tidal bulge of Mars raised by Phobos and Phobos' actual position on its orbit.

A possible way to represent the viscoelastic behavior of Mars is to treat the Love numbers and the gravimetric factor as complex variables (e.g., Moore & Schubert, 2000): the ratio between their imaginary part and their real part is then a function of the dissipation factor:

$$\frac{1}{Q_{\ell mpq}} = \frac{\Im(k_{\ell mpq})}{\Re(k_{\ell mpq})} \tag{12}$$

This highlights the frequency dependency for the geometric lag angle and the tidal amplitude. The dissipation factor Q is highly dependent of the frequency (Bagheri et al., 2019; Efroimsky & Lainey, 2007), while the amplitude of gravimetric factors through the Love numbers is less dependent (Khan et al., 2018; Nimmo & Faul, 2013). As the term $\ell = m$ has the greatest amplitude, when talking about amplitude, we will focus on the main period T_ℓ corresponding to the degree ℓ. Thus, we will use the simplified notation δ_ℓ for the gravimetric factor $\delta_{\ell\ell}$ (equal to $\delta_\ell(T_\ell)$).

To get the tidal response of Mars to Phobos, we computed the complex Love numbers k and h up to degree 4 for the three set of models described in Section 3. We derived their respective gravimetric factors, and calculated the expected amplitude of the tidal response of Mars to the tidal potential of Phobos by taking their absolute value, shown in Figure 2. Because most of the gravity changes at the surface of Mars from Phobos is due to its direct attraction, the phase lag of the gravimetric factor is much smaller than the geometric lag angle. This means that the maximal gravity change from the Phobos tides will be only very slightly off from the tidal potential of Phobos.

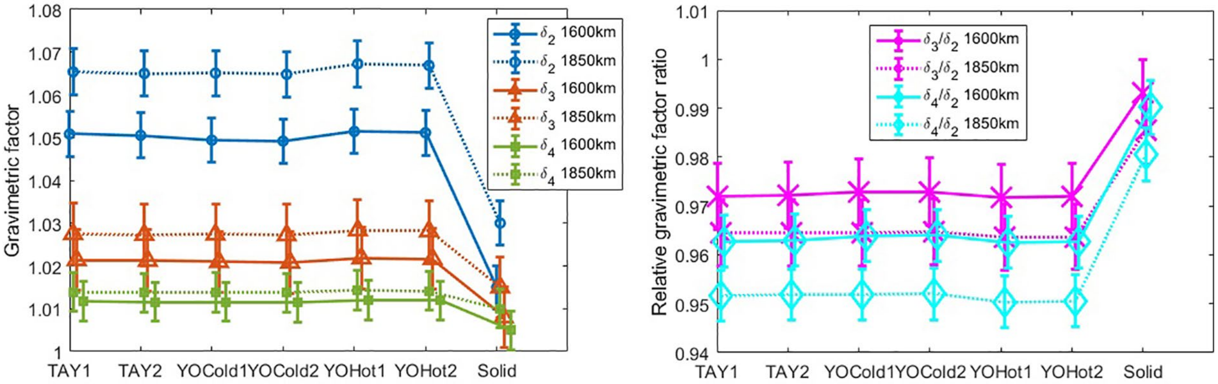

Figure 2. Absolute (a) and relative ratio (b) of the gravimetric factor for degree 2, 3, and 4 Phobos tides for the three sets of models described in Section 3. Solid core gravimetric factors are significantly smaller than liquid core ones. Cold mantle models also tend to have smaller gravimetric factors than hot mantle models. Error bars are from accuracy given in Table 3.

Besides constraining the interior of Mars with the gravimetric factors for each separate degree, another possibility described in Lognonné et al. (2019) is to study the ratio between the gravimetric factors. While this requires a more complex measurement compared to only measuring the degree 2 (the signal with the highest amplitude [Pou et al., 2018]) this method does not need an absolute calibration of the gravimeter, hence may be more accurate. Figure 2 shows the ratio between the amplitudes of either degree 3 and degree 2, or degree 4 and degree 2 for the three sets of models. The values of the gravimetric factors in Figure 2 are given in Table 2.

5. Noise Model and Expected SEIS Output

Prior to InSight's arrival on Mars, noise models had already been developed for SEIS, such as Pou et al. (2016), Murdoch, Kenda, et al. (2017), Murdoch, Mimoun, et al. (2017), Mimoun et al. (2017). While these studies were mainly focused on the seismic range between 0.01 and 100 Hz (Lognonné et al., 2019), low frequency noises were the focus of Pou et al. (2018). Thermal noise has been identified as the dominant source of noise, followed by pressure noise. Because of how large these noise contributions were expected to be, noise decorrelation was assumed necessary to retrieve the Phobos tides from the SEIS VBB POS (position) data, whose output is the most suitable one for long period analysis (Pou et al., 2018). As seen in Figure 1b, the amplitude of the modeled Phobos tide signal is less than 2×10^{-8} m.s^{-2}, which is smaller than the resolution of the SP seismometer of 6.7×10^{-5} m.s^{-2} on its best output (MPOS) at tidal frequencies (Lognonné et al., 2019). Therefore, we expect that only the VBB seismometer on InSight will be able to detect it on its

Table 2
Values of the Gravimetric Factors and Their Ratio Shown in Figure 2 Based on the Martian Models Described in Section 3

Parameter for given core size	TAY1	TAY2	YOCold1	YOCold2	YOHot1	YOHot2	Solid
δ_2 (1,600 km)	1.0508	1.0505	1.0494	1.0492	1.0515	1.0512	1.015
δ_2 (1,850 km)	1.0654	1.0650	1.0651	1.0648	1.0673	1.0669	1.03
δ_3 (1,600 km)	1.0214	1.0212	1.0209	1.0208	1.0218	1.0216	1.008
δ_3 (1,850 km)	1.0275	1.0273	1.0274	1.0272	1.0283	1.0281	1.015
δ_4 (1,600 km)	1.0117	1.0116	1.0116	1.0115	1.0120	1.0119	1.005
δ_4 (1,850 km)	1.0139	1.0137	1.0138	1.0137	1.0143	1.0142	1.01
δ_3/δ_2 (1,600 km)	0.9720	0.9721	0.9729	0.9729	0.9718	0.9719	0.9931
δ_3/δ_2 (1,850 km)	0.9644	0.9646	0.9646	0.9647	0.9635	0.9637	0.9854
δ_4/δ_2 (1,600 km)	0.9628	0.9629	0.9639	0.9640	0.9625	0.9627	0.9901
δ_4/δ_2 (1,850 km)	0.9516	0.9518	0.9518	0.9520	0.9504	0.9506	0.9806

scientific position output, as its resolution on high gain should be better than 3×10^{-11} m.s^{-2} (Lognonné et al., 2019).

The first results from InSight show the SEIS noise performance is even better than expected based on on-Earth tests, with a noise level slightly above 10^{-10} m.s^{-2}.Hz$^{-1/2}$ at a period of a few seconds for the VBB seismometer, measured in the early evening when the atmosphere is still (Banerdt et al., 2020). Atmospheric data have also been recorded with unprecedented continuity and accuracy, and are in accordance with previous prediction and modeling (Banfield et al., 2020). This is of particular interest for this study, as environmental noise from the atmosphere is the main noise source for the seismic sensors (Lognonné et al., 2020), and has been postulated to be the same at low frequencies (Pou et al., 2018). Here, we wish to remodel the environmental low frequency noises as measured by SEIS with the updated continuous atmospheric data from InSight. For the instrument self-noise levels, given the better than expected performances of SEIS, we will keep the noise data from Earth-based tests used from Mimoun et al. (2017), and used for instance in Clinton et al. (2017) or Pou et al. (2018).

In previous studies, the preferred method to model the thermal noise was to use measurements from previous Martian missions (Lognonné et al., 2019; Van Hoolst et al., 2003), and to use global circulation models to estimate the pressure at the InSight landing site (Murdoch, Kenda, et al., 2017; Murdoch, Mimoun, et al., 2017). While Mars Pathfinder was near the Martian equator like InSight (Schofield et al., 1997), both the temperature and pressure data recorded lack continuity over a whole Martian year (roughly equal to 2 Earth years), thus the preference for the Viking Lander 2 data (Murphy et al., 1990). Now, with the arrival of the InSight lander, we have access to the continuous temperature and pressure data of the Martian atmosphere with a better continuity and time sampling compared to previous missions (Banfield et al., 2020). However, as InSight has only been on-site since November 2019, it has not recorded yet the data for a full Martian year. The solution implemented here was to use the InSight measurements for the temperature and pressure instead where both the data were continuous, interpolate them to have a time sampling of 1 s and extrapolate them with a convolution with the Viking 2 data trend over 2 Earth years (one Martian year). Examples of the data are accessible in (Banfield et al., 2020) or in Figure 4.

Thermal noise is modeled according to the previous works of Mimoun et al. (2017) and Pou et al. (2018), by filtering the atmospheric temperature with two first-order low pass filters. The first one represents the WTS, the Wind and Thermal Shield protecting the SEIS instrument, with a time constant of 7.2 h. The second represents the sphere/Remote Warm Enclosure Box (RWEB), the part where the SEIS VBB seismometers are, with a time constant of 3 h. To this filtered temperature, representing the most accurate temperature sensor (the SCIT, scientific temperature), a phase lag τ_{lag}^{0} of 10 h is added to model the propagation delay between the outside of the sphere (inside the RWEB) where the SCIT sensor is, and the inside of the sphere where the SEIS VBB seismometers are. Finally, the thermal noise as seen by the seismometer is given by multiplying the phase-lagged temperature to the thermal sensitivity of the VBB α assumed constant (Mimoun et al., 2017), as shown in Equation 13:

$$n_{thermal} = \alpha\, T_{SCIT}\left(t - \tau_{lag}^{0}\right) \tag{13}$$

Following the works of Pou et al. (2018), three different effects are considered to model the pressure noise. The first one is atmospheric loading: as the atmosphere causes a forcing on the Martian surface, the ground moves and creates a surface tilt signal that can be seen by a seismometer (Murdoch, Kenda, et al., 2017; Sorrels, 1971). The second one is the free air anomaly effect: as mentioned in Lognonné and Clévédé (2002), an accelerometer at the surface of a planetary body also sees acceleration on its vertical axis caused by a vertical ground displacement of the planetary surface due to the atmosphere. This phenomenon grows stronger at very low frequencies and therefore must be considered in our case; however, as modeled in Pou et al. (2018), it is still smaller than the atmospheric loading at the diurnal frequency of 1.1×10^{-5} Hz and therefore also at the main Phobos tide frequency ($\ell = 2$ for $f = 50$ μHz). Lastly, the atmosphere above the gravimeter exerts a gravitational attraction on the instrument (Beauduin et al., 1996; Spiga et al., 2018; Zürn & Widmer, 1995); the sum of all these three effects were added as pressure noise in the model.

We add all the previous mentioned noise sources (thermal noise, pressure noise, and instrumental noises) with the tidal response of Mars calculated in Section 4 to create a synthetic acceleration input that SEIS is

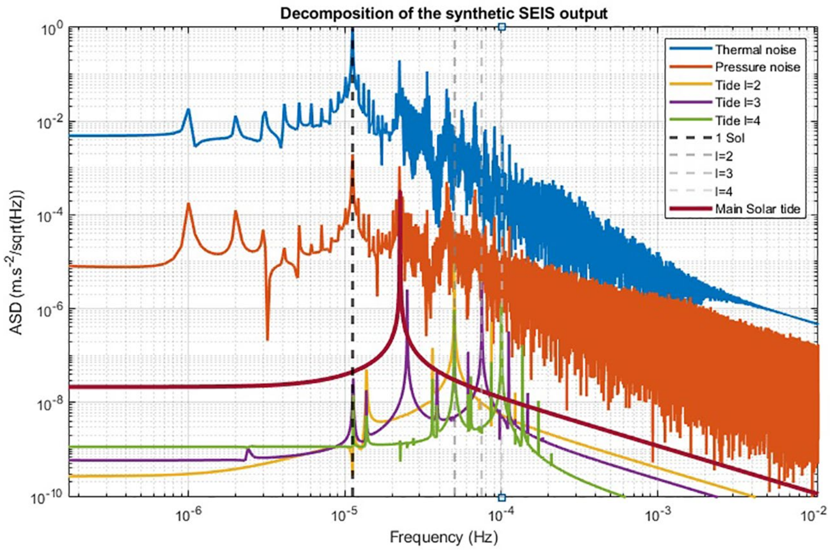

Figure 3. Amplitude spectral density of the decomposition of the main contributions of the synthetic Seismic Experiment for Interior Structure Output: thermal noise model, pressure noise model and Phobos tidal signals. Both thermal noise and pressure noise must be corrected before being able to resolve the Phobos tides. The reference tidal lines have a finite width due to windowing and instrument response. Vertical dotted lines denote tidal periods.

expected to see at the surface of Mars; we also add the main $\ell = 2$ Solar tide, as the main Phobos tide is only 8% of the Solar tide amplitude (Van Hoolst et al., 2003). The response of the VBB seismometer is taken from the SEIS metadata available on the Geosciences node of the NASA PDS in order to simulate the SEIS synthetic output that we will get from the insight mission over its nominal duration. The result is shown in Figure 3, giving similar results compared to the previous works of Pou et al. (2018) and the gravity changes calculated in Section 4 for each separate tidal degree. Both this work and those of Pou et al. (2018) yield a similar amplitude spectrum which is to be expected as the InSight data are in good accordance with the previous missions data and modeling (Banfield et al., 2020). It is also clear that the Phobos tidal signal will be challenging to recover from the SEIS output, as the signal-to-noise ratio of its strongest component, the degree-2 tide, is close to 10^{-5}. This being the case, we will explain in the following section our proposed methodology to extract the Phobos tides from this synthetic SEIS output.

6. Synthetic Data Inversion

The first step of the inversion is to convert the synthetic SEIS output into the acceleration at the surface of Mars. This is done by using the VBB transfer function available as the metadata through IRIS or the NASA PDS Geosciences node. Because we are focusing on long period signals, the VBB output of interest is the VBB POS output, here assumed to be at High Gain. However, subtracting the instrument response from the VBB output is not enough to get the tidal acceleration of Mars, since the seismometer is also sensitive to various noise sources. Because of how strong they are compared to our tidal signals, these noise sources have to be removed using noise decorrelation.

Similar to what was done in Pou et al. (2018), we will use the fact that we have a lot of information on the noise seen by SEIS thanks to the temperature and pressure sensors, and that we also know the shape of the Phobos tides signal from the Phobos ephemerides and the forward modeling done in Sections 2 and 4. Therefore, the favored method here is to use matched filters (Turin, 1960). The first one is in order to correct the phase lag τ_{lag} between the temperature sensor SCIT and the temperature of the VBB seismometer, which is the direct cause of the modeled thermal noise seen. This is done by maximizing the correlation between the synthetic SEIS output from Section 5 and the temperature from the SEIS temperature sensor:

$$\tau_{lag} = \max_{\tau} \int_{-\infty}^{+\infty} Output_{SEIS} * T_{SCIT}(t-\tau)dt \qquad (14)$$

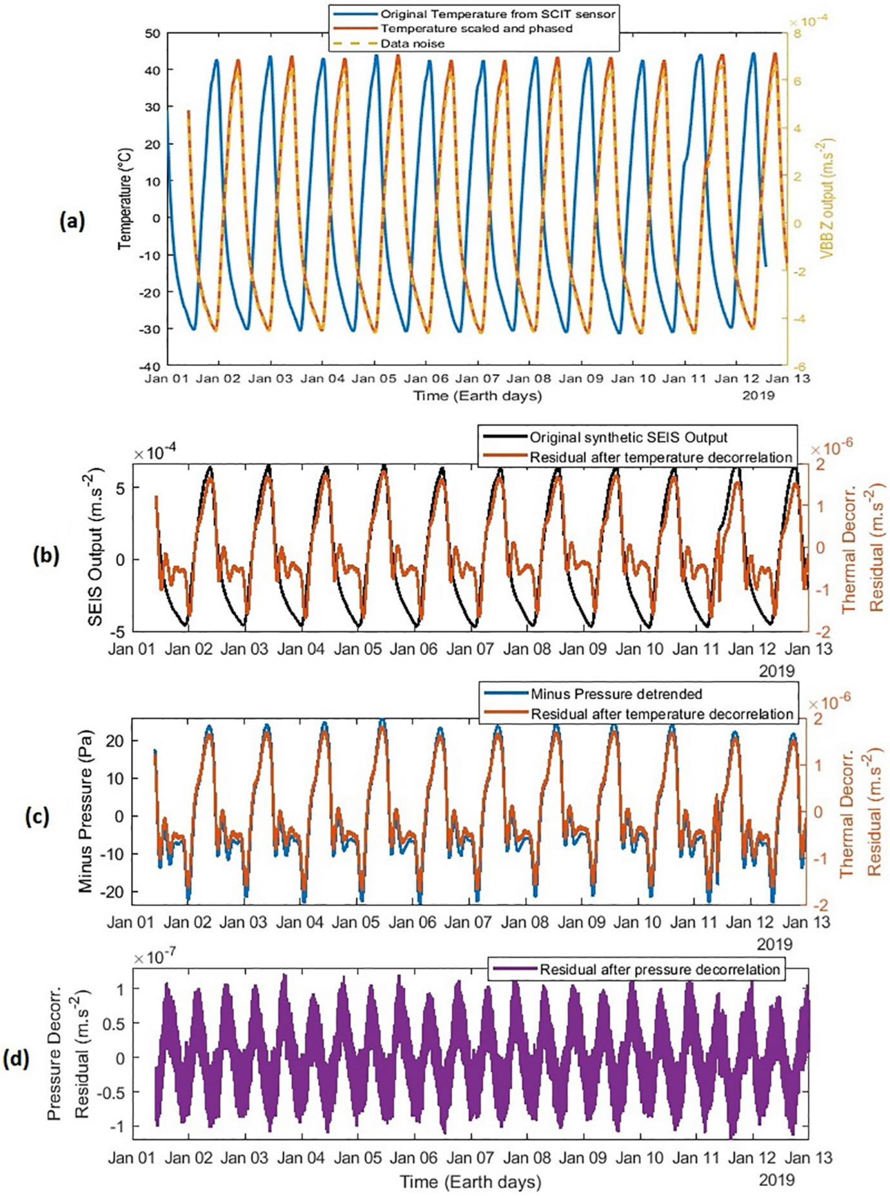

Figure 4. Illustration of the noise decorrelation process. (a) Application of the matched filter to correct the temperature phase lag with the thermal noise seen by the Very Broad Band seismometer. Solid lines are temperatures, while dotted line is our synthetic Seismic Experiment for Interior Structure (SEIS) output. While the plot only shows data for about 2 Earth weeks, the filter is run over the 2 years to get the aforementioned accuracy of 0.02%. (b) Synthetic SEIS output compared to the result of the thermal noise decorrelation using the filter described in Equation 15. (c) Comparison between the result of the thermal noise decorrelation and the atmospheric pressure shows as expected a high correlation between the two signals. (d) Residual after pressure decorrelation using an least mean square adaptive filter.

where $Output_{SEIS}$ is our synthetic SEIS output and T is the temperature given by the SCIT sensor. The various signals and results are shown in Figure 4. With 2 years of data, the implemented phase lag of 10 h is recovered with an accuracy of 0.02%.

Once the phase lag is corrected, thermal noise decorrelation is performed by trying to find the thermal sensitivity α of the VBB seismometer. This is done by using another matched filter:

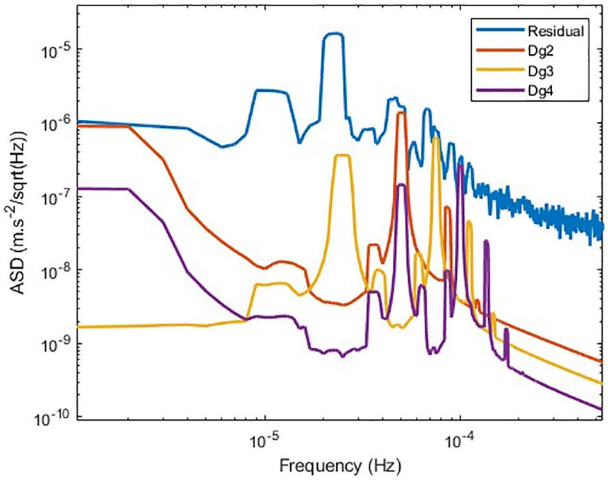

Figure 5. Amplitude spectral density of the residual after temperature and pressure decorrelation, and of the Phobos tides of degree 2, 3, and 4. In order to reduce artifacts from windowing and interpolations in gaps, a Thomson multitaper has been applied.

$$VBB_{sensitivity} = \max_{\alpha} \left| \int_{-\infty}^{+\infty} pressure(t) * \text{diff}(\alpha,t)dt \right| \tag{15}$$

$$\text{diff}(\alpha,t) = Output_{SEIS}(t) - \alpha T_{SCIT}(t-\tau_{lag}) \tag{16}$$

where α is the estimation of the VBB thermal sensitivity and τ_{lag} our estimation of τ_{lag}^{0} from Equation 13 with the matched filter from Equation 14.

The input of the matched filter is made of two components. The first one is the pressure from the InSight pressure sensors, used as a reference to what the output should look like. The second part is a differential signal (called diff in Equation 15) equal to the synthetic SEIS Output (data noise in Figure 4) minus our estimation of the VBB thermal noise. This noise is assumed to be equal to a α parameter (representing the VBB thermal sensitivity) times the temperature corrected by the phase lag found from the previous matched filter (temperature called "Temperature scaled and phased" in Figure 4). The value of α is determined as the value that creates the output the most similar to the pressure measurements.

The main advantage of this technique is to guarantee that pressure noise decorrelation will be possible after the thermal noise decorrelation. This may not be the case when using other filtering techniques such as least mean square (LMS) filtering since both pressure and temperature are highly correlated due to similar diurnal variations. Because only the pressure variations around the Phobos tidal frequency range are of interest to us, the pressure has been high-pass filtered with a cut-off period of one month. The result of this second matched filter is shown in Figure 4a. Since the matched filter is designed to maximize the correlation between the differential signal and the pressure, the residual is as expected very close to the pressure signal in shape as seen in Figure 4b.

Pressure decorrelation at seismic frequencies has been studied before the InSight landing in Murdoch, Kenda, et al. (2017), where using an LMS adaptive filter yielded good results. The same method was also used in Pou et al. (2018), with similar results. Therefore, we will use the same method for the pressure decorrelation. Since pressure noise is the last major noise to correct before seeing the Phobos tides (see Mimoun et al., 2017; Pou et al., 2018, and Figure 3), the precautions used for the temperature decorrelation are not required. The result of such filtering is shown in Figure 4c: as expected, the residual is very similar to a tidal signal of degree 2. This is not the main Phobos tide, but the main Solar tide, as its amplitude is more than 10 times stronger than the main Phobos tides.

As the residual is dominated by the Solar tide, one might think that retrieving the solar gravimetric factor of Mars is easier. This is not the case because the main Solar tide is highly correlated with the diurnal noise sources and their harmonics. Although the noise decorrelations were effective, they were not perfect and altered the Solar tides while reducing the noise levels. This is less the case for the Phobos tides, since their frequency range is distinct from the diurnal harmonics (Lognonné et al., 1996; Van Hoolst et al., 2003), as shown in Pou et al. (2018). The gravimetric factor recovery can be found by calculating the spectrum of both the residual and the expected tidal potential of Phobos from Section 2, and calculating the ratio of the respective spectra at the Phobos tidal frequencies (see Figure 5).

However, such a method has its limits. As the degree 2 Phobos tide has only a cosine term in $\cos(2S)$ (see Equation 8), one might believe taking the Fourier transform of the output at the $\ell = 2$ period of 5 h 33 min will yield the gravimetric factor δ_2. This is not the case, because the degree 4 of the Phobos tide also presents a term in $\cos(2S)$ (see Equation 9), and therefore the ratio of the spectra at the $\ell = 2$ period of 5 h 33 min will be impacted by the $\ell = 4$ tides and thus δ_4 too. This is clearly visible in Figure 5, where the amplitude of Dg2 (degree 2 Phobos tide) is noticeably less than the amplitude of the residual at its main frequency. A solution is to use once again a matched filter like the one used for the temperature decorrelation (see Equation 15), but with the differential signal being the residual after all decorrelations minus the potential of the $\ell = 2$

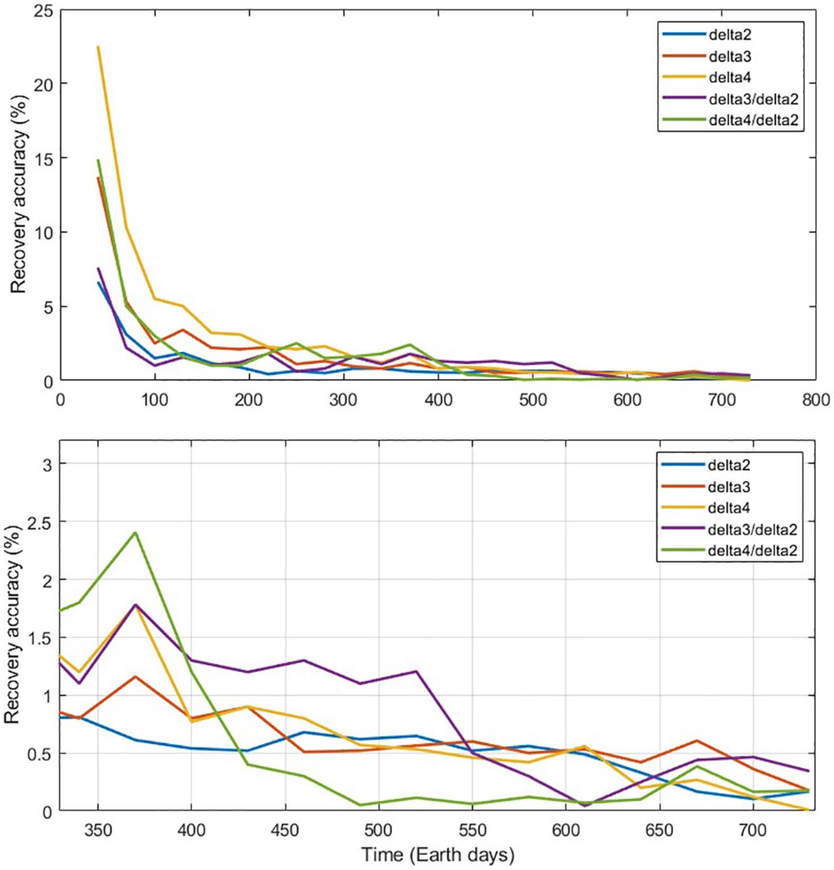

Figure 6. Accuracy in the retrieval of the gravimetric factor δ_ℓ for the Phobos tides of degree $\ell = 2$, $\ell = 3$ and $\ell = 4$. Top plot is over 2 Earth years, while bottom plot shows the second year's worth of data. This is the error due to the noise remaining after the inversion process.

Phobos tide times the gravimetric factor δ_ℓ, and maximizing its correlation with the Phobos tidal potential at $\ell = 3$ as this degree does not have a cosine with a period of 19,980 s.

The matched filter obtained is:

$$\delta_2 = \max_{\delta} \left| \int_{-\infty}^{+\infty} V_3 * diff(\delta,t)dt \right| \tag{17}$$

$$diff(\delta,t) = Residual(t) - \delta\Delta g_\ell(t) \tag{18}$$

with Δg_ℓ being the terms of the change in gravity in Equation 3 separated by degree.

The same formula can be used for determining δ_4 with V_4, while for δ_3, the correlation can be maximized when using V_2 times the differential function. The results over time of this method are given in Figure 6: the accuracy of the absolute gravimetric factors after two Earth years is better than 0.3%, 0.6%, and 0.2% respectively for δ_2, δ_3, and δ_4, while the relative gravimetric ratios are better than 0.5% for δ_3/δ_2 and 0.3% for δ_4/δ_2 (see Figure 6).

7. Sensitivity Study

The results shown in Figure 6 assuming that everything is known with a perfect precision, and linear effects. But, besides the inversion errors due to the noises seen by SEIS, other errors have to be taken into account in our inversion study, as they will also impede the recovery of the true gravimetric factors of Mars at the Phobos tides periods.

In order to retrieve the gravimetric factors of Mars under the forcing of Phobos, we recovered the local gravity variations as seen by SEIS based on Equation 3, which can be rewritten to make the tidal potential of Phobos more explicit:

$$\begin{aligned}\Delta g(r_{mars}) &= \sum_{\ell=2}^{\infty} \delta_\ell \left(\ell g_0 \frac{m^*}{m_{Mars}} \left(\frac{r_{mars}}{a^*} \right)^{\ell+1} P_\ell\left(\cos S\right) \right) \\ &= \sum_{\ell=2}^{\infty} \delta_\ell\, \ell \left(\frac{Gm^*}{a^{*2}} \left(\frac{r_{mars}}{a^*} \right)^{\ell-1} P_\ell\left(\cos S\right) \right) \\ &= \sum_{\ell=2}^{\infty} \delta_\ell \frac{\mathrm{d}}{\mathrm{d}r} \left(\frac{Gm^*}{a^*} \left(\frac{r_{mars}}{a^*} \right)^{l} P_\ell\left(\cos S\right) \right) \\ &= \sum_{\ell=2}^{\infty} \delta_\ell \frac{\mathrm{d}V_\ell}{\mathrm{d}r}(r_{mars})\end{aligned} \tag{19}$$

where r_{mars} is the Martian radius at the InSight lander location. The local gravity variations seen by SEIS are in a frequency range where the VBB POS transfer function can be considered as a single gain (Lognonné et al., 2019). Therefore, the relation between the SEIS output and the actual gravity variations at the surface of Mars can be written:

$$\Delta g(r) = \frac{Output_{SEIS}}{Gain_{SEIS}} \tag{20}$$

$Gain_{SEIS}$ is the absolute gain of SEIS. In Pou et al. (2018), the authors estimated a possible recovery of this absolute quantity with a relative error of 0.4% for the calibration method they devised; we will take the same value. The complete expression for the calculation of a degree ℓ gravimetric factor is:

$$\delta_\ell = \frac{Output_{SEIS}}{Gain_{SEIS} * \left(\ell \left(\frac{Gm^*}{a^{*2}} \left(\frac{r_{mars}}{a^*} \right)^{\ell-1} P_\ell\left(\cos S\right) \right) \right)} \tag{21}$$

Equation 21 is differentiated to determine the worst-case total error on the gravimetric factor:

$$\begin{aligned}\frac{\Delta\delta_\ell}{\delta_\ell} = &\frac{\Delta Output_{SEIS}}{Output_{SEIS}} + \frac{\Delta Gain_{SEIS}}{Gain_{SEIS}} \\ &+ \frac{\Delta(Gm^*)}{Gm^*} + (\ell-1)\frac{\Delta r_{mars}}{r_{mars}} + (\ell+1)\frac{\Delta a}{a} \\ &+ \frac{\Delta P_\ell\left(\cos S\right)}{P_\ell\left(\cos S\right)}\end{aligned} \tag{22}$$

The first term refers to our decorrelation process detailed in Section 6. The second term is the error determined in Pou et al. (2018), estimated to be possibly constrained around 0.4%. The four terms left are linked to the ephemerides of Phobos and Mars, and to the actual position of SEIS and the InSight lander on Mars.

7.1. Error Determination

While the error due to our decorrelation process depends on the time spent on accumulating the data (see Section 6 and Figure 6), the other errors present in Equation 22 can be evaluated beforehand. First, the error on the SEIS gain is assumed here to be at 0.4%, based on the estimations from Pou et al. (2018).

The position of SEIS has been accurately determined by a combination of remote imaging from orbiters and Doppler-based radio science with the RiSE experiment aboard InSight (Golombek et al., 2020). Given the HiRiSE accuracy of about 25 cm per pixel, this translates into a latitude and longitude error of respectively less than 0.0055% and 0.000025% (McEwen et al., 2010).

Recent flybys by Mars Express close to Phobos constrained its mass down to 1.5% error (Pätzold et al., 2014), but distant flybys were also considered resulting in a conservative estimation. If only taking into account the close flybys, the Phobos mass estimation can be as low as 0.3% error on the mass (Andert et al., 2010), and secular evolution models of the orbit of Phobos can even reduce it to less than 0.1% (Konopliv et al., 2006; Rosenblatt et al., 2008). As such, we will consider a middle ground of the estimation of the Phobos mass from the close flybys around 0.5%. Using these mass estimations, the ephemerides of Phobos have been refined, with errors on the distance between Phobos and Mars down to 2 km and 30 millidegrees for the inclination and declination. This means relative errors of 0.03% on the distance and 0.04% on the angles (Jacobson et al., 2018). These errors might also be further reduced with future planned missions to Phobos such as MMX (Campagnola et al., 2018).

7.2. Gravimetric Factor Recovery

When estimating the gravimetric factors separately for each degree, all the errors in Equation 22 must be taken into account. The main contributors are then the error due on the gain of SEIS, with an assumed value here of 0.4% and the error in the mass of Phobos, evaluated at 0.5%. However, these two errors can be canceled when estimating the gravimetric factor ratios, as they are the same for every gravimetric factor. In that case, the dominant error is due to the inversion process. This error is smaller the more data are accumulated, and is also smaller for degree 2 and degree 3 as they are the biggest tidal signals. Considering all these errors, we can update Table 2 with our estimations of the recovery of the gravimetric factors of Mars at the Phobos tides frequencies (Table 2).

The first column is derived from the maximal uncertainty still permitting differentiation between the 6 first models (liquid core) and the last one (solid core) in Figure 2 and Table 2. The second column is made assuming a Martian liquid core (as favored by the k_2^s measurements) as the maximal uncertainty allowing differentiation between the dotted lines (core size of 1,850 km) and the solid lines (core size of 1,600 km), thus giving a possible core size estimation better than 1,725 ± 125 km.

From these values, our conclusion is that a total data duration of two Earth years should be enough to determine δ_2 and δ_2/δ_4 with sufficient accuracy to constrain both the state of the core and its size with a margin of 125 km.

7.3. Phase Lag Recovery

As both the amplitude and the phase lag of the gravity variations induced by the Phobos tides are helpful to constrain the Martian interior, we also tried to recover the phase lag with various noise decorrelation methods. However, because of how small it is ($Q_{22}^{p} = 100$ equals a time lag of about 32 s), we did not manage to recover the phase lag and the quality factor Q with an accuracy better than the range of 80–105 that we choose for this study.

Two main methods were tested: the first one was a similar matched filter as given in Equation 15 for the recovery of the thermal phase lag, but applied to the residuals from Equation 17 after all noise decorrelations for each tidal degree at their main frequencies. The second one was to use stacking over a Martian sol of all the gravimetric signals, and try to do a Bayesian inversion based on a Random Walk Monte-Carlo algorithm to try to recover both amplitude and phase lag of the tides, while using noise-free data from the

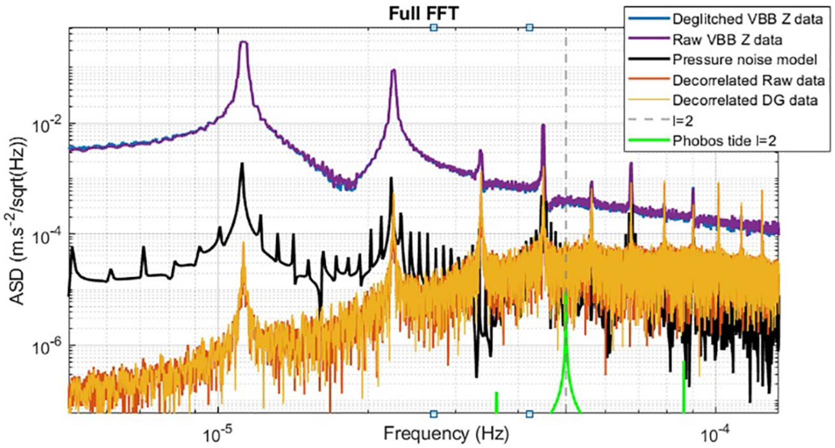

Figure 7. Amplitude spectral density of the Seismic Experiment for Interior Structure output data and the residual after thermal decorrelation compared to synthetic pressure noise from our model in Figure 3 and the Phobos main tide ($l = 2$) spectrum. Data shown here are between June and December 2020. The pressure noise model is similar to or lower than the residual spectrum because the current least mean square decorrelation partially correct pressure effects too as they are highly correlated to temperature. Peaks at high frequencies in the residual are due to the solar harmonics being amplified due to the temperature power of 2 and 3 used. DG data means data without glitches (for deglitched), while raw data are data with glitches still present.

Phobos ephemerides as a priori constraints. But because of interference between the cosine frequencies and the small phase lags, neither of these methods managed to get an accuracy on Q_{22}^{p} better than 50 with a time sampling of 1 s on the data after 2 years, and was even worse for the other quality factors Q_{33}^{p} and Q_{44}^{p}. As a consequence, we do not expect to be able to get additional constraints on the Martian interior from the phase lag of the Phobos tides induced gravity variations.

8. Discussion

The data processing described above has also been tested on the real SEIS data (available from the InSight Mars SEIS Data Service, 2019). As we do not have yet a full Martian year of data, we did not expect the inversion process on the real data to be currently able to see the Phobos tides precisely enough to actually constrain the interior structure of Mars.

Processing of the actual data turned out to be much more challenging than theoretical models due to various effects. Glitches (Scholz et al., 2020) are seen by SEIS as steps in acceleration and therefore adding noise at all frequencies, so they must be corrected. Thermoelastic effects inside SEIS due to deformations of the ring supporting the sphere where the VBB seismometer is located also made the thermal decorrelation more complicated, as the scientific temperature is close to a sine wave, while all three VBB outputs are not. The VBB thermal sensitivity is also itself a function of temperature (see Lognonné et al., 2019). Ground temperature modeling as a possible source of thermal noise creating a ground tilt has also been studied based on the works of Siegler et al. (2017), but has been found to be much weaker than the signal observed. The heater activation for the Martian winter in May 2019 also made it complicated to combine the data before and after the activation, as the temperature range changed a lot and so did the thermal noise. Similarly, because of increasing noise in the Martian atmosphere starting in February 2020, the VBB TCDM (Thermal Compensation Device Mechanism) had to be modified causing major changes in the VBB response in May 2020. In this study, we hence focused our efforts on the data between June 2019 and May 2020.

Current decorrelation efforts use the scientific temperature SCIT channel together with the VBB temperature channels, in phase with the VBB POS outputs but their resolution is much worse. To retrieve the temperature sensitivity of the VBB thermal sensitivity, the inversion uses a LMS fit between each separate VBB output with the SCIT and the VBB temperature, with the last one being considered at the power one, squared, and cubed. We did not go beyond the power 3, because the power 4 of the temperature would have a frequency

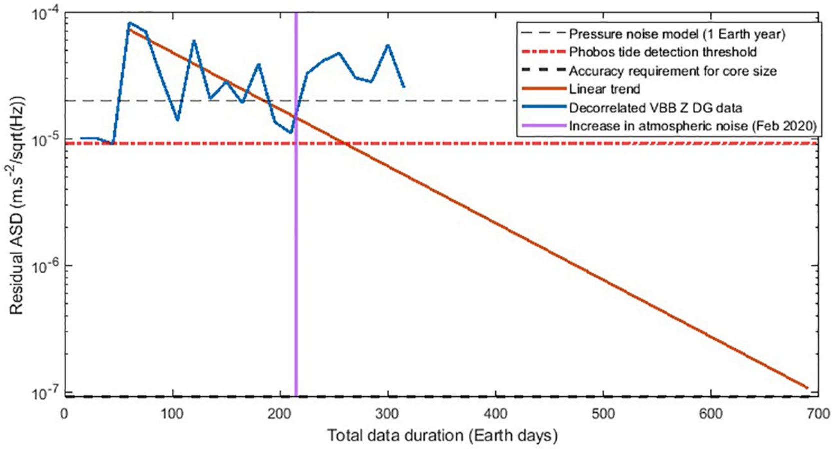

Figure 8. Thermal decorrelation results of the Seismic Experiment for Interior Structure output data over time and future prevision with linear fit. Data range is between June 2019 and May 2020. The expected accuracy for recovering δ_2 to the accuracy to get the core size was expected be reached after 2 Earth years' worth of data based on the initial trend (for data from June 2019 to January 2020), but stronger atmospheric noise likely due to the Martian dust storm season have delayed it. The first data points look very good, but this is because the least mean square fit is too good when only having a few days worth of data and deletes a lot of signal without making the Phobos tides apparent. While the current thermal decorrelation results are worse than the synthetic data decorrelation results in Figure 6, they are currently without pressure decorrelation which should greatly improve residuals.

close to the main Phobos tide (44 μHz compared to 50 μHz), and we wanted to avoid removing relevant signal as much as possible. To model the changes in the VBB thermal response, fits were done on a Sol-to-Sol basis. Because the thermal decorrelation is currently done by a LMS fit over each Sol separately, pressure decorrelation is not yet feasible. As more data become available, temperature decorrelation should yield better results over the whole range of the data, which would allow us to also decorrelate the pressure-related signals.

Results of the decorrelation for the data between June and December 2019 are shown in Figure 7, where we can see that the residual of the temperature decorrelation reduced the noise level by around two orders of magnitude at the main Phobos tide frequency, down to approximately the level of noise the atmospheric pressure is expected to be at. Deglitched data, noted DG in the figure, have slightly less noise than the raw data as expected, but on long durations do not appear to change the impact of the temperature decorrelation as both spectra of the decorrelated deglitched data and decorrelated raw data are similar. Alternative methods in time domain such as stacking and only considering the evening and night data (as they have a much lower noise level, Banerdt et al., 2020) are also being investigated but with no results so far.

The trend of noise reduction is shown in Figure 8. We expected to be able to distinguish between models using the Phobos tides after at least after two Earth years based on the data between June 2019 and January 2020, but increasing atmospheric noise starting in February 2020 may delay it. However, the results here are shown with only thermal noise decorrelation. While the current residual spectrum is below the expected pressure noise, this is because the LMS fit on the temperature also corrects pressure effects due to the high correlation between temperature and pressure; however, pressure effects cannot be corrected together with the temperature using a LMS fit as was shown in Pou et al. (2018) and verified with our updated synthetic noise model. As time goes by, thermal noise decorrelation will improve and pressure noise decorrelation should also be possible, likely improving our residual for an earlier detection of the Phobos tides. If this is confirmed and the theoretical results given in Table 3 are confirmed, then SEIS should be able to resolve the state of the core and its size with an accuracy better than ±125 km when using either the absolute amplitude of δ_2 for the $\ell = 2$ tide, or the relative ratio between δ_4 and δ_2.

Table 3
Accuracy Needed to Constrain the State of the Size of the Core of Mars, From the Gravimetric Factors Shown in Figure 2 Based on the Models Described in Section 3, With Estimated Parameter Recovery Errors

Parameter	Accuracy needed for the state of the core (%)	Accuracy needed for the size of the core ±125 km (%)	Parameter recovery after 2 Earth years (%)
δ_2	3.4	1.2	1.1
δ_3	1.2	0.5	1.4
δ_4	0.4	0.2	1.0
δ_3/δ_2	2.0	0.8	1.3
δ_4/δ_2	2.2	1.2	1.1

More accurate Martian models may also be possible by combining these SEIS measurements with subsurface observations, as InSight has been doing with dust devils and probing the upper crust with crustal reflected waves (Lognonné et al., 2020). Deeper constraints may be possible through analysis of the first marsquakes (Giardini et al., 2020; Lognonné et al., 2020). The precession and nutation of Mars (Dehant et al., 2012) and the Chandler Wobble (Konopliv et al., 2020) could also provide additional information on the deep Martian structure.

Data Availability Statement

The Phobos ephemerides data used in this paper are available on the JPL Horizons website https://ssd.jpl.nasa.gov/horizons.cgi. All SEIS data can be found under the reference https://doi.org/10.18715/SEIS.INSIGHT.XB_2016 for the seismic and atmospheric data from the InSight mission. The Viking 2 data used are available from the NASA PDS atmospheres node at the following depository: https://pds-atmospheres.nmsu.edu/cgi-bin/getdir.pl?dir=data&volume=vl_1001.

Acknowledgments
This work is supported in part by the NASA InSight participating scientist program (NNH17ZDA001N-INSTP-SP). The French Team acknowledges support from the French Space Agency CNES, CNRS, and ANR (ANR-14-CE36-0012-02 and ANR-19-CE31-0008-08). We acknowledge NASA, CNES, their partner agencies, and Institutions (UKSA, SSO, DLR, JPL, IPGP-CNRS, ETHZ, IC, MPS-MPG) and the flight operations team at JPL, SISMOC, MSDS, IRIS-DMC, and PDS for providing SEED SEIS data. This paper is InSight contribution number 190. A. R. acknowledges the support of the Belgian PRODEX program managed by the European Space Agency in collaboration with the Belgian Federal Science Policy Office.

References

Agnew, D. C. (2007). Earth tides. In Treatise on geophysics (Vol. 3, pp. 163–195). Elsevier B. V. https://doi.org/10.1016/b978-044452748-6/00056-0

Andert, T. P., Rosenblatt, P., Pätzold, M., Häusler, B., Dehant, V., Tyler, G. L., & Marty, J. C. (2010). Precise mass determination and the nature of Phobos. *Geophysical Research Letters*, *37*(9). https://doi.org/10.1029/2009GL041829

Bagheri, A., Khan, A., Al-Attar, D., Crawford, O., & Giardini, D. (2019). Tidal response of mars constrained from laboratory-based viscoelastic dissipation models and geophysical data. *Journal of Geophysical Research: Planets*, *124*(11), 2703–2727. https://doi.org/10.1029/2019JE006015

Banerdt, W. B., Smrekar, S. E., Banfield, D., Giardini, D., Golombek, M., Johnson, C. L., & Wieczorek, M. (2020). Initial results from the insight mission on mars. *Nature Geoscience*, *13*(3), 183–189. https://doi.org/10.1038/s41561-020-0544-y

Banfield, D., Spiga, A., Newman, C., Forget, F., Lemmon, M., Lorenz, R., & Banerdt, W. B. (2020). The atmosphere of mars as observed by insight. *Nature Geoscience*, *13*(3), 190–198. https://doi.org/10.1038/s41561-020-0534-0

Beauduin, R., Lognonné, P., Montagner, J. P., Cacho, S., Karczewski, J. F., & Morand, M. (1996). The effects of the atmospheric pressure changes on seismic signals or how to improve the quality of a station. *Bulletin of the Seismological Society of America*, *86*(6), 1760.

Beuthe, M. (2015). Tidal love numbers of membrane worlds: Europa, titan, and co. *Icarus*, *258*, 239–266. https://doi.org/10.1016/j.icarus.2015.06.008

Bills, B. G., Neumann, G. A., Smith, D. E., & Zuber, M. T. (2005). Improved estimate of tidal dissipation within Mars from MOLA observations of the shadow of Phobos. *Journal of Geophysical Research*, *110*(E7). https://doi.org/10.1029/2004JE002376

Boynton, W. V., Feldman, W. C., Mitrofanov, I. G., Evans, L. G., Reedy, R. C., Squyres, S. W., & Ton'chev, A. K. (2004). The mars odyssey gamma-ray spectrometer instrument suite. In C. T. Russell (Ed.), *2001 Mars Odyssey*, (pp. 37–83). Springer Netherlands. https://doi.org/10.1007/978-0-306-48600-5_2

Campagnola, S., Yam, C. H., Tsuda, Y., Ogawa, N., & Kawakatsu, Y. (2018). Mission analysis for the Martian Moons Explorer (MMX) mission. *Acta Astronautica*, *146*, 409–417. https://doi.org/10.1016/j.actaastro.2018.03.024

Clinton, J. F., Giardini, D., Lognonné, P., Banerdt, B., van Driel, M., Drilleau, M., & Spiga, A. (2017). Preparing for InSight: An invitation to participate in a blind test for Martian seismicity. *Seismological Research Letters*, *88*(5), 1290–1302. https://doi.org/10.1785/0220170094

Dehant, V., Banerdt, B., Lognonné, P., Grott, M., Asmar, S., Biele, J., & Vennerstrøm, S. (2012). Future Mars geophysical observatories for understanding its internal structure, rotation, and evolution. *Planetary and Space Science*, *68*(1), 123–145. https://doi.org/10.1016/j.pss.2011.10.016

Dehant, V., Defraigne, P., & Wahr, J. M. (1999). Tides for a convective Earth. *Journal of Geophysical Research*, *104*(B1), 1035–1058. https://doi.org/10.1029/1998JB900051

Dreibus, G., & Wanke, H. (1985). Mars, a volatile-rich planet. *Meteoritics*, *20*, 367–381.

Efroimsky, M., & Lainey, V. (2007). Physics of bodily tides in terrestrial planets and the appropriate scales of dynamical evolution. *Journal of Geophysical Research*, *112*(E12). https://doi.org/10.1029/2007JE002908

Efroimsky, M., & Makarov, V. V. (2013). Tidal friction and tidal lagging. applicability limitations of a popular formula for the tidal torque. *The Astrophysical Journal*, *764*(1), 26. https://doi.org/10.1088/0004-637x/764/1/26

Faul, U. H., & Jackson, I. (2007). Diffusion creep of dry, melt-free olivine. *Journal of Geophysical Research*, *112*(B4). https://doi.org/10.1029/2006JB004586

Folkner, W. M., Yoder, C. F., Yuan, D. N., Standish, E. M., & Preston, R. A. (1997). Interior structure and seasonal mass redistribution of Mars from radio tracking of Mars pathfinder. *Science*, *278*(5344), 1749–1752. https://doi.org/10.1126/science.278.5344.1749

Giardini, D., Lognonné, P., Banerdt, W. B., Pike, W. T., Christensen, U., Ceylan, S., & Yana, C. (2020). The seismicity of Mars. *Nature Geoscience*, *13*(3), 205–212. https://doi.org/10.1038/s41561-020-0539-8

Golombek, M., Warner, N. H., Grant, J. A., Hauber, E., Ansan, V., Weitz, C. M., & Banerdt, W. B. (2020). Geology of the insight landing site on Mars. *Nature Communications*, *11*(1), 1014. https://doi.org/10.1038/s41467-020-14679-1

InSight Mars SEIS Data Service. (2019). *SEIS raw data, Insight Mission* (IPGP, JPL, CNES, ETHZ, ICL, MPS, ISAE-Supaero, LPG, MFSC). https://doi.org/10.18715/SEIS.INSIGHT.XB_2016

Jacobson, R. A., Konopliv, A. S., Park, R. S., & Folkner, W. M. (2018). The rotational elements of Mars and its satellites. *Planetary and Space Science*, *152*, 107–115. https://doi.org/10.1016/j.pss.2017.12.020

Jacobson, R. A., & Lainey, V. (2014). Martian satellite orbits and ephemerides. *Planetary and Space Science*, *102*, 35–44. https://doi.org/10.1016/j.pss.2013.06.003

Kaula, W. M. (1964). Tidal dissipation by solid friction and the resulting orbital evolution. *Reviews of Geophysics*, *2*(4), 661–685. https://doi.org/10.1029/RG002i004p00661

Khan, A., Liebske, C., Rozel, A., Rivoldini, A., Nimmo, F., Connolly, J. A. D., & Giardini, D. (2018). A geophysical perspective on the bulk composition of Mars. *Journal of Geophysical Research: Planets*, *123*(2), 575–611. https://doi.org/10.1002/2017JE005371

Konopliv, A. S., Asmar, S. W., Folkner, W. M., Karatekin, O., Nunes, D. C., Smrekar, S. E., & Zuber, M. T. (2011). Mars high resolution gravity fields from MRO, Mars seasonal gravity, and other dynamical parameters. *Icarus*, *211*(1), 401–428. https://doi.org/10.1016/j.icarus.2010.10.004

Konopliv, A. S., Park, R. S., & Folkner, W. M. (2016). An improved JPL Mars gravity field and orientation from Mars orbiter and lander tracking data. *Icarus*, *274*, 253–260. https://doi.org/10.1016/j.icarus.2016.02.052

Konopliv, A. S., Park, R. S., Rivoldini, A., Baland, R.-M., Le Maistre, S., Van Hoolst, T., & Dehant, V. (2020). Detection of the chandler wobble of mars from orbiting spacecraft. *Geophysical Research Letters*, *47*(21), e2020GL090568. https://doi.org/10.1029/2020GL090568

Konopliv, A. S., Yoder, C. F., Standish, E. M., Yuan, D.-N., & Sjogren, W. L. (2006). A global solution for the Mars static and seasonal gravity, Mars orientation, Phobos and Deimos masses, and Mars ephemeris. *Icarus*, *182*(1), 23–50. https://doi.org/10.1016/j.icarus.2005.12.025

Lainey, V., Dehant, V., & Pätzold, M. (2007). First numerical ephemerides of the Martian moons. *Astronomy & Astrophysics*, *465*(3), 1075–1084. https://doi.org/10.1051/0004-6361:20065466

Lognonné, P., Banerdt, W. B., Giardini, D., Pike, W. T., Christensen, U., Laudet, P., & Wookey, J. (2019). SEIS: Insight's seismic experiment for internal structure of mars. *Space Science Reviews*, *215*(1), 12. https://doi.org/10.1007/s11214-018-0574-6

Lognonné, P., Banerdt, W. B., Pike, W. T., Giardini, D., Christensen, U., Garcia, R. F., & Zweifel, P. (2020). Constraints on the shallow elastic and anelastic structure of mars from insight seismic data. *Nature Geoscience*, *13*(3), 213–220. https://doi.org/10.1038/s41561-020-0536-y

Lognonné, P., Beyneix, J. G., Banerdt, W. B., Cacho, S., Karczewski, J. F., & Morand, M. (1996). Ultra broad band seismology on InterMars-Net. *Planetary and Space Science*, *44*(11), 1237–1249. https://doi.org/10.1016/S0032-0633(96)00083-9

Lognonné, P., & Clévédé, E. (2002). Normal modes of the Earth and Planets. *International Geophysics*, *81*, 125. https://doi.org/10.1016/s0074-6142(02)80213-3

Lognonné, P., & Mosser, B. (1993). Planetary seismology. *Surveys in Geophysics*, *14*, 239–302. https://doi.org/10.1007/BF00690946

Love, A. E. H. (1911). Some problems of geodynamics (Vol. 1). Cambridge University Press.

MacDonald, G. J. F. (1964). Earth and moon: Past and future. *Science*, *145*(3635), 881–890. https://doi.org/10.1126/science.145.3635.881

McEwen, A. S., Banks, M. E., Baugh, N., Becker, K., Boyd, A., Bergstrom, J. W., & Wray, J. J. (2010). The High Resolution Imaging Science Experiment (HiRISE) during MRO's Primary Science Phase (PSP). *Icarus*, *205*(1), 2–37. https://doi.org/10.1016/j.icarus.2009.04.023

McSween, H. Y. (1994). What we have learned about Mars from SNC meteorites. *Meteoritics*, *29*(6), 757–779. https://doi.org/10.1111/j.1945-5100.1994.tb01092.x

Mimoun, D., Murdoch, N., Lognonné, P., Hurst, K., Pike, W. T., Hurley, J., & Banerdt, W. B. (2017). The Noise Model of the SEIS Seismometer of the InSight Mission to Mars. *Space Science Reviews*, *211*, 383–428. https://doi.org/10.1007/s11214-017-0409-x

Moore, W. B., & Schubert, G. (2000). The tidal response of Europa. *Icarus*, *147*(1), 317–319. https://doi.org/10.1006/icar.2000.6460

Murdoch, N., Kenda, B., Kawamura, T., Spiga, A., Lognonné, P., Mimoun, D., & Banerdt, W. B. (2017). Estimations of the seismic pressure noise on Mars determined from Large Eddy Simulations and demonstration of pressure decorrelation techniques for the InSight mission. *Space Science Reviews*, *211*(1–4), 457–483. https://doi.org/10.1007/s11214-017-0343-y

Murdoch, N., Mimoun, D., Garcia, R., Rapin, W., Kawamura, T., Lognonné, P., & Banerdt, B. (2017). Evaluating the wind-induced mechanical noise on the InSight seismometers. *Space Science Reviews*, *211*, 429–455. https://doi.org/10.1007/s11214-016-0311-y

Murphy, J. R., Leovy, C. B., & Tillman, J. E. (1990). Observations of Martian surface winds at the Viking lander 1 site. *Journal of Geophysical Research*, *95*(B9), 14555–14576. https://doi.org/10.1029/JB095iB09p14555

Murray, C. D., & Dermott, S. F. (2000). *Solar system dynamics*.

Nimmo, F., & Faul, U. H. (2013). Dissipation at tidal and seismic frequencies in a melt-free, anhydrous mars. *Journal of Geophysical Research: Planets*, *118*(12), 2558–2569. https://doi.org/10.1002/2013JE004499

Pätzold, M., Andert, T. P., Tyler, G. L., Asmar, S. W., Häusler, B., & Tellmann, S. (2014). Phobos mass determination from the very close flyby of Mars Express in 2010. *Icarus*, *229*, 92–98. https://doi.org/10.1016/j.icarus.2013.10.021

Plesa, A.-C., Padovan, S., Tosi, N., Breuer, D., Grott, M., Wieczorek, M. A., & Banerdt, W. B. (2018). The thermal state and interior structure of Mars. *Geophysical Research Letters*, *45*(22), 12198–12209. https://doi.org/10.1029/2018GL080728

Pou, L., Mimoun, D., Garcia, R. F., Lognonné, P., Banerdt, W. B., Karatekin, O., & Zhu, P. (2016). Mars deep internal structure determination using Phobos tide measurement strategy with the SEIS/InSight experiment. In EGU General Assembly Conference Abstracts (Vol. 18, pp. EPSC2016–8724).

Pou, L., Mimoun, D., Lognonne, P., Garcia, R. F., Karatekin, O., Nonon-Latapie, M., & Llorca-Cejudo, R. (2018). High precision SEIS calibration for the insight mission and its applications. *Space Science Reviews*, *215*(1), 6. https://doi.org/10.1007/s11214-018-0561-y

Redmond, J. C., & Fish, F. F. (1964). The luni-tidal interval in Mars and the secular acceleration of Phobos. *Icarus*, *3*(2), 87–91. https://doi.org/10.1016/0019-1035(64)90048-X

Rivoldini, A., Van Hoolst, T., Verhoeven, O., Mocquet, A., & Dehant, V. (2011). Geodesy constraints on the interior structure and composition of Mars. *Icarus*, *213*(2), 451. https://doi.org/10.1016/j.icarus.2011.03.024

Rosenblatt, P., Lainey, V., Le Maistre, S., Marty, J. C., Dehant, V., Pätzold, M., & Häusler, B. (2008). Accurate Mars Express orbits to improve the determination of the mass and ephemeris of the Martian moons. *Planetary and Space Science*, *56*(7), 1043–1053. https://doi.org/10.1016/j.pss.2008.02.004

Samuel, H., Lognonné, P., Panning, M., & Lainey, V. (2019). The rheology and thermal history of mars revealed by the orbital evolution of Phobos. *Nature*, *569*(7757), 523–527. https://doi.org/10.1038/s41586-019-1202-7

Schofield, J. T., Barnes, J. R., Crisp, D., Haberle, R. M., Larsen, S., Magalhães, J. A., & Wilson, G. (1997). The Mars Pathfinder Atmospheric Structure Investigation/Meteorology (ASI/MET) Experiment. *Science*, *278*(5344), 1752–1758. https://doi.org/10.1126/science.278.5344.1752

Scholz, J.-R., Widmer-Schnidrig, R., Davis, P., Lognonné, P., Pinot, B., Garcia, R. F., & Banerdt, W. B. (2020). Detection, analysis, and removal of glitches from insight's seismic data from mars. *Earth and Space Science*, *7*(11), e2020EA001317. https://doi.org/10.1029/2020EA001317

Seidelmann, P. K., Archinal, B. A., A'hearn, M. F., Conrad, A., Consolmagno, G. J., Hestroffer, D., & Williams, I. P. (2007). Report of the IAU/IAG Working Group on cartographic coordinates and rotational elements: 2006. *Celestial Mechanics and Dynamical Astronomy*, *98*(3), 155–180. https://doi.org/10.1007/s10569-007-9072-y

Shida, T. (1912). On the body tides of the Earth, a proposal for the International Geodetic Association. *Proceedings of the Tokyo Mathematico-Physical Society, 2nd Series*, *6*(16), 242–258. https://doi.org/10.11429/ptmps1907.6.16_242

Siegler, M. A., Smrekar, S. E., Grott, M., Piqueux, S., Mueller, N., Williams, J.-P., & Spohn, T. (2017). The insight mars lander and its effect on the subsurface thermal environment. *Space Science Reviews*, *211*(1), 259–275. https://doi.org/10.1007/s11214-017-0331-2

Smrekar, S. E., Lognonné, P., Spohn, T., Banerdt, W. B., Breuer, D., Christensen, U., & Wieczorek, M. (2018). Pre-mission insights on the interior of Mars. *Space Science Reviews*, *215*(1), 3. https://doi.org/10.1007/s11214-018-0563-9

Sorrells, G. G. (1971). A preliminary investigation into the relationship between long-period seismic noise and local fluctuations in the atmospheric pressure field. *Geophysical Journal International*, *26*(1–4), 71–82. https://doi.org/10.1111/j.1365-246X.1971.tb03383.x

Spiga, A., Banfield, D., Teanby, N. A., Forget, F., Lucas, A., Kenda, B., & Banerdt, W. B. (2018). Atmospheric science with insight. *Space Science Reviews*, *214*(7), 109. https://doi.org/10.1007/s11214-018-0543-0

Stacey, F. (1969). *Physics of the earth* (p. 324). John Wiley & Sons.

Taylor, G. J. (2013). The bulk composition of Mars. *Chemie der Erde - Geochemistry*, *73*(4), 401–420. https://doi.org/10.1016/j.chemer.2013.09.006

Taylor, P. A., & Margot, J.-L. (2010). Tidal evolution of close binary asteroid systems. *Celestial Mechanics and Dynamical Astronomy*, *108*(4), 315–338. https://doi.org/10.1007/s10569-010-9308-0

Turin, G. (1960). An introduction to matched filters. *IRE Transactions on Information Theory*, *6*(3), 311–329. https://doi.org/10.1109/TIT.1960.1057571

Van Hoolst, T., Dehant, V., Roosbeek, F., & Lognonné, P. (2003). Tidally induced surface displacements, external potential variations, and gravity variations on Mars. *Icarus*, *161*(2), 281–296. https://doi.org/10.1016/S0019-1035(02)00045-3

Yoder, C. F., Konopliv, A. S., Yuan, D. N., Standish, E. M., & Folkner, W. M. (2003). Fluid core size of Mars from detection of the solar tide. *Science*, *300*(5617), 299–303. https://doi.org/10.1126/science.1079645

Yoshizaki, T., & McDonough, W. F. (2020). The composition of mars. *Geochimica et Cosmochimica Acta*, *273*, 137–162. https://doi.org/10.1016/j.gca.2020.01.011

Zürn, W., & Widmer, R. (1995). On noise reduction in vertical seismic records below 2 mHz using local barometric pressure. *Geophysical Research Letters*, *22*(24), 3537–3540. https://doi.org/10.1029/95GL03369